Small

NANO · MICRO small
www.small-journal.com

RESEARCH ARTICLE

A Soft and Robust Liquid Metal Textile Platform for Versatile Bioelectronic Applications

Yang Wang[1,2] | Bochuan Jiang[1] | Chang Ding[3] | Junhua Zheng[1] | Peihua Xu[2] | Huanyu Yang[2] | Chengkuo Lee[2] | Yu Jiang[4] | Yuhang Li[1,5]

[1]Institute of Solid Mechanics School of Aeronautic Science and Engineering, Beihang University, Beijing, China | [2]Department of Electrical and Computer Engineering, National University of Singapore, Singapore, Singapore | [3]School of Materials Science and Engineering, Beihang University, Beijing, China | [4]Engineering Research Center of Bone and Joint Precision Medicine, Ministry of Education, Peking University Third Hospital, Beijing, China | [5]Ningbo Innovation Research Institute of Beihang University, Ningbo, China

Correspondence: Chengkuo Lee (elelc@nus.edu.sg) | Yu Jiang (jiangyu@bjmu.edu.cn) | Yuhang Li (liyuhang@buaa.edu.cn)

Received: 27 November 2025 | **Revised:** 29 January 2026 | **Accepted:** 9 February 2026

Keywords: flexible electronics | human-machine interaction | liquid metal | smart textile | wearable heater

ABSTRACT

Wearable bioelectronic systems are rapidly emerging as a core technological platform for next-generation health monitoring, neuromodulation, and human–machine interaction. These applications impose stringent demands on materials, including softness, high electrical conductivity, conformal skin contact, and long-term durability. In this work, we present an ultrathin, highly customizable, and encapsulation-free smart textile platform based on a liquid metal (LM) and waterborne polyurethane composite. The conductive patterns are fabricated via laser pre-patterning and a one-step heat-transfer printing process, without the need for additional adhesives or encapsulation layers, enabling high-resolution integration with textile substrates. The resulting fabric electrodes exhibit outstanding initial conductivity, excellent mechanical stretchability, and robust wash durability over multiple laundering cycles. This textile platform supports a wide range of bioelectronic functionalities, including high-fidelity electrocardiogram (ECG) signal acquisition, rapid and tunable Joule heating for wearable warming applications, lightweight neural network-based gesture recognition (ten classes), and electrical stimulation for pain relief or functional therapy. Together, these results offer a unified, multifunctional platform for next-generation wearable devices and intelligent textile systems.

1 | Introduction

Flexible electronics have become an essential foundation for the expanding field of wearable technologies, supporting diverse applications in health monitoring, motion tracking, rehabilitation, and human-machine interaction [1–4]. Next-generation wearable systems are expected not only to exhibit excellent mechanical compliance but also to maintain stable and accurate functionality under continuous deformation, repeated washing, and complex environments [5–8]. To meet the increasing demand for multidimensional sensing and active feedback, there is a pressing need to move from single-function devices toward multifunctional integration, which calls for more versatile and scalable solutions in terms of materials, device structures, and fabrication processes [9–12].

Among various flexible electronic systems, electronic textiles have emerged as ideal platforms for creating long-term, skin-conformable, and breathable wearable systems [13–16]. Thanks to their wearability and compatibility with large-area fabrication, textile-based electronics have attracted considerable interest [17–19]. In recent years, a variety of functional e-textiles have been developed through printing [20, 21], transfer printing [22], coating [23, 24], and textile-based integration techniques

[25], enabling flexible incorporation of electronic functionalities into fabric substrates. These developments have enabled diverse applications including strain and pressure sensing, electrophysiological signal acquisition, thermal regulation, and electrical stimulation [26–29]. Such progress has accelerated the evolution from individual components to fully integrated wearable systems, and laid important groundwork for practical deployment [30–32].

Recent advances in smart textiles have extended wearable biomedical systems far beyond conventional electrophysiological electrodes, encompassing optoelectronic, photothermal, and energy-harvesting functionalities [33–35]. Hwang et al. reported a stretchable fiber-based OLED display enabled by robust, conductive, and deformable via structures, achieving stable operation under large mechanical deformation [36]. Sohn et al. demonstrated printed fabric-based OLEDs using a poly(vinyl alcohol) planarization layer to improve electrode uniformity and device performance [37]. Qiu et al. introduced an alignment-free textile sensing sleeve that integrates ECG and impedance plethysmography for comprehensive cardiovascular assessment, reducing sensitivity to sensor positioning while maintaining high signal fidelity [38]. Tang et al. developed a Janus textile with tunable photothermal heating modes through asymmetric material integration, enabling environment-adaptive personal thermal regulation [39]. Hou et al. further demonstrated fabric-assisted flexible thermoelectric generators capable of harvesting body heat under large deformation for a wearable energy supply [40]. While these studies highlight the broad functional diversity achievable in textile-based platforms, many of the optically driven or structurally specialized approaches rely on complex interconnect architectures, asymmetric coatings, or precise structural control, which may limit scalability, robustness, and system-level integration [41].

LMs such as Galinstan have gained attention for their unique combination of high electrical and thermal conductivity, mechanical fluidity, and biocompatibility [42, 43]. LMs have been increasingly applied in textile-based devices to support applications in flexible circuits, pressure sensors, thermal heaters, and bio signal interfaces [44–46]. LMs can be incorporated onto fabric surfaces via injection, coating, or printing methods, enabling functions such as temperature control, motion sensing, and ECG acquisition [47, 48]. However, challenges remain in achieving high-resolution patterning, durable adhesion to textile substrates, and stable conductivity over multiple washing cycles. Building LM-based textile systems that integrate conformal patterning, strong interfacial bonding, and reliable multifunctionality remains a key research direction.

To better position this work within the current landscape of textile-based conductive patterning technologies, Table 1 summarizes representative strategies reported in previous studies, including solution impregnation, wet spinning, electroless metallization, helical wire wrapping, and liquid-metal-based composites. As shown in Table 1. In this work, we offer a simple and scalable fabrication route that enables laser-defined patterning with good spatial resolution, while simultaneously maintaining high electrical conductivity and excellent stretchability. This combination of processing simplicity, patterning fidelity, and electromechanical performance.

We introduce a conductive polyurethane membrane system reinforced with LM and carbon nanotubes, and establish a rapid fabrication approach that combines laser pre-patterning with single-step thermal transfer printing in Figure 1. This process allows the formation of stable conductive patterns on textile substrates without the need for additional encapsulation layers. The resulting textile architecture exhibits enhanced pattern precision, robust mechanical durability, and large-scale processability. Based on this method, we present a unified smart textile platform capable of supporting a range of bioelectronic functions, including high-fidelity ECG monitoring, fast-response heating, electrical stimulation through skin-integrated arrays, and wearable gesture recognition based on lightweight neural networks. This study demonstrates a complete system from material design to functional validation, showing the platform's adaptability to various application scenarios in physiological monitoring, interactive control, and personalized therapy. It provides an integrated, scalable, and flexible pathway toward the development of next-generation wearable bioelectronic systems.

2 | Materials and Methods

2.1 | Preparation of Conductive Ink

During ink preparation, 1 mL of liquid metal (≈6.3 g) was first mixed with 10 mL of ethanol (volume ratio 1:10) and ultrasonically treated for 5 min using a bath sonicator (40% power, 300 W) to break the bulk LM into micro- and nanoscale droplets and form a stable oxide shell, yielding a uniform core-shell dispersion.

A commercial waterborne TPU dispersion (38 wt.% solid content) was subsequently added as the elastic matrix and adhesive phase. The resulting LM/TPU (solid) mass ratio was approximately 6.3:3.8, corresponding to an LM loading of ~62 wt.% with respect to the total solid content. CNT, pre-dispersed in ethanol (0.1 g CNT in 10 mL ethanol via 5 min ultrasonication), were introduced in a controlled amount to reinforce the conductive network and enhance mechanical robustness without significantly affecting ink viscosity.

After a brief defoaming and stirring step (15 s), a homogeneous and bubble-free conductive ink was obtained, with a final solid content of approximately 25–30 wt.%, suitable for blade coating. The ink was coated onto a PET substrate to form an elastic film (~50 μm thick) and cured at 50°C prior to laser patterning and thermal transfer.

2.2 | Preparation of CNT Dispersion

CNT (0.1 g) was added to 10 mL of ethanol and ultrasonicated for 5 min to form a stable dispersion. The volume of CNT dispersion added to the ink was calculated based on a preset ratio.

2.3 | Fabrication and Patterning of Conductive Elastomer Films

The conductive ink was blade-coated onto a PET substrate to a thickness of approximately 50 μm and thermally cured at 50°C

TABLE 1 | Summary of conductive patterning technologies for textile-based electronics.

Conductive Materials	Method	Patterning Resolution	Encapsulation	Advantages	Ref.
PDA/CNT/PPy-modified cotton fabric	Solution impregnation	Not patterned	Hydrophobic coating	Integrated triboelectric layer and electrode	[49]
Ag NPs/MXene on cotton	Solution impregnation of Ag NPs/MXene	Not patterned	PDMS overlayer	High electrical conductivity; improved durability under bending,	[50]
$Ti_3C_2T_x$ MXene/GQDs/PANI fibers	Microfluidic wet spinning and chemical assembly with in situ polymerization	Not patterned	Not encapsulated	High electrochemical performance; hierarchical fiber architecture;	[51]
Electroless-metallized PA textile	Electroless metallization with PDMS embedding and laser patterning	Laser-defined patterns	PDMS	High electrical and thermal conductivity; excellent stretchability; multifunctional textile platform	[52]
Enamelled Cu wires on elastic yarn	Helical wrapping of Cu wires around an elastic core	Weave-defined line patterns	UV-curable polymers; silicone tubing	Precise temperature sensing; good durability under stretching,	[53]
Liquid metal/fluoropolymer composite	Hot pressing	Simple cut-out patterns	Fluoropolymer-enhanced polymer matrix	Washable; high air and moisture permeability; good biocompatibility	[44]
CNT/LM /TPU	Laser cutting and hot pressing	~100 μm	Not encapsulated	Simple and scalable fabrication; good patterning fidelity; high electrical conductivity; excellent stretchability and mechanical robustness	This work

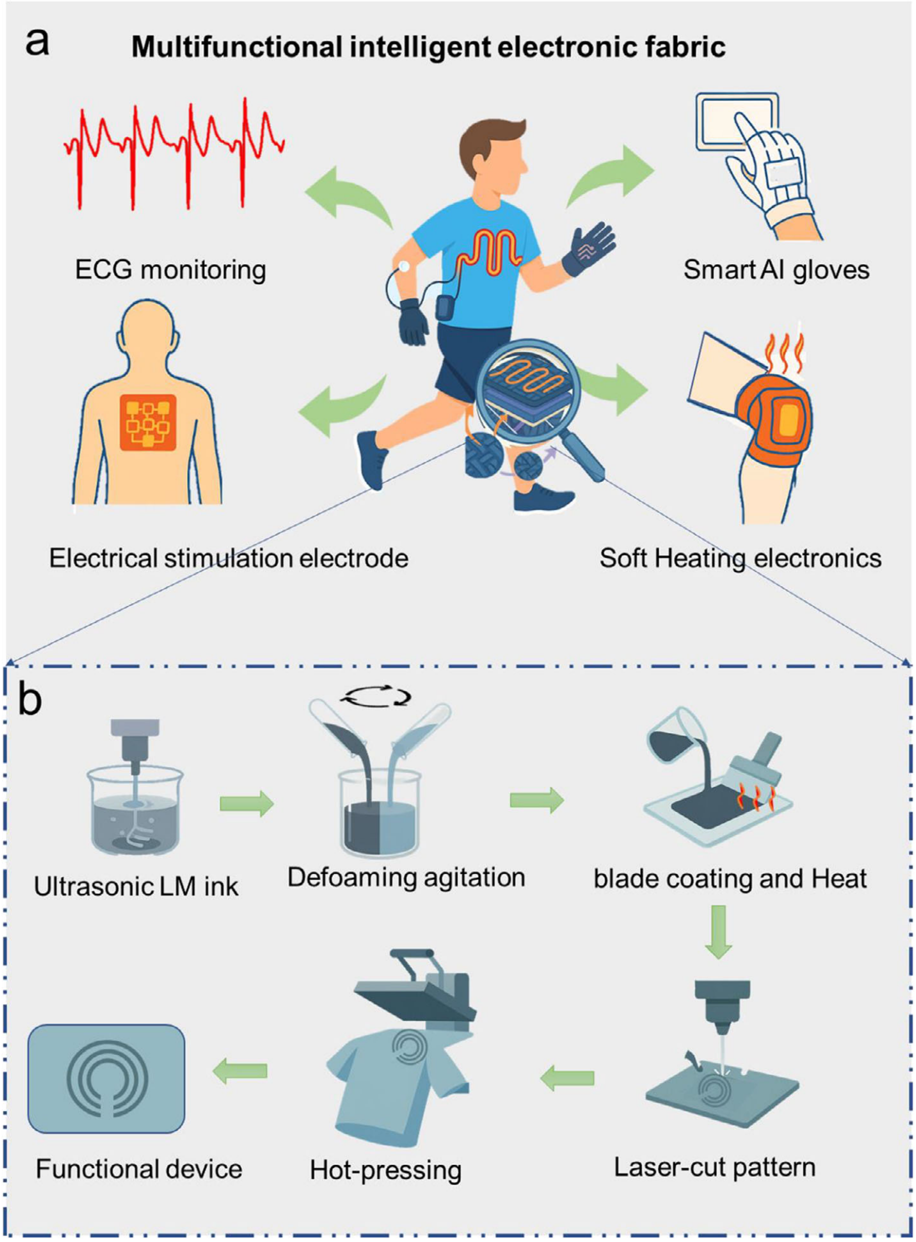

FIGURE 1 | Schematic illustration of the multifunctional smart textile and its fabrication process. (a) Application scenarios of the patterned conductive textile include ECG monitoring, thermal heating, electrical stimulation, and gesture recognition. (b) Scalable and precise fabrication workflow.

to form an elastic conductive film. Laser cutting was used to create patterned features, which were then laminated with textile substrates and hot-pressed at 90 °C for 50 min. After cooling, the PET layer was peeled off to obtain patterned conductive textiles. All electrodes, wearable devices, and gloves described in this work were fabricated using this method.

2.4 | Mechanical and Electrical Performance Testing

Patterned textile samples were cut into strips of 50 mm × 5 mm. The overall textile thickness was ~500 μm, and the conductive layer was ~50 μm thick. Tensile testing was performed to assess strain responsiveness, and electrical resistance was recorded under different strain states to evaluate electromechanical coupling behavior.

2.5 | Wash Durability Evaluation

Wash durability was first evaluated using a controlled laboratory protocol to ensure repeatability. Specifically, samples were immersed in 1000 mL of water containing 2 mL of household detergent and stirred using a glass rod for 3 min, followed by rinsing with clean water for 30 s. Each cycle was defined as one washing process. Electrical resistance was measured before and after multiple washing cycles to assess conductive stability.

In addition, to better simulate practical manual laundering conditions encountered during daily wear, a representative hand

-washing process was performed, including direct rinsing under running water, manual rubbing with detergent, thorough rinsing, and air drying. The corresponding procedure is provided in Video S3. As shown in the video, the conductive patterns remain intact throughout the washing process, with no visible cracking, delamination, edge lifting, or pattern breakage, further confirming the robustness of the conductive layer under realistic washing conditions.

2.6 | Material Characterization

The surface morphology and interfacial embedding of the conductive patterns on the textile were observed using scanning electron microscopy (SEM, model EM-30+). Samples were gold-sputtered prior to imaging to improve conductivity. SEM imaging was performed at an accelerating voltage of 15 kV to analyze the uniformity and adherence of the CNT/LM/TPU composite layer.

Additionally, Fourier transform infrared spectroscopy (FTIR, model Tensor II) was used to investigate molecular interactions and functional groups within the composite film, scanning from 400 to 4000 cm^{-1} to characterize LM, CNT, and TPU components.

2.7 | Biocompatibility Evaluation

NIH-3T3 fibroblasts were used to assess the biocompatibility of the textile samples. Three groups were prepared (Blank, LM/TPU, CNT/LM/TPU). For each group, a 2 mm × 2 mm fabric sample was placed in a 15 mm well. After a 24-h pre-culture period, the sample was added and co-cultured for an additional 24 h. Cell viability was assessed by DAPI staining and nuclear counting.

2.8 | Heating Performance Test

The textile heaters were powered by a DC supply with controlled voltage/current input. Surface temperature rise and heat distribution were recorded using an infrared thermal imaging camera.

2.9 | Gesture Recognition Experiment

Patterned conductive fabrics were sewn into a five-finger glove to form a five-channel sensing array. Signals were collected using a microcontroller during different hand gestures. Each gesture type was recorded more than 120 times, and both time-domain and frequency-domain features were extracted for neural network classification.

2.10 | ECG Acquisition

Fabric electrodes were shaped and placed at standard chest positions to collect ECG signals. Data were recorded via a microcontroller platform under both resting and motion conditions. This study was ethically reviewed by the Medical Science Research Ethics Committee of Peking University Third Hospital, with the approval number IRB00006761-M2023727, and the informed consent of the experimental volunteers was obtained.

2.11 | Electrical Stimulation Experiment

The textile electrodes were attached to the forearm skin and connected to a medical electrical stimulator. Simultaneously, a bio-potential acquisition system recorded the surface voltage response to evaluate stimulation transmission capability. This study was ethically reviewed by the Medical Science Research Ethics Committee of Peking University Third Hospital, with the approval number IRB00006761-M2023727, and the informed consent of the experimental volunteers was obtained.

3 | Results and discussion

3.1 | Process Design and Structural Optimization of the Smart Textile

To construct a patterned smart textile platform with excellent conductivity, flexibility, and stable wearability, we developed a scalable and high-precision fabrication process (Figure 1b). This process includes the preparation of LM-based conductive ink, formation of ultrathin conductive films, laser patterning, thermal transfer printing, and final textile device assembly.

During ink preparation, ultrasonic treatment was used to break the LM into micro- and nanoscale particles and form a stable oxide shell, resulting in a uniform core–shell dispersion. TPU was then added to serve as an elastic matrix and adhesive phase, enabling the conductive particles to be embedded in the polymer network. This provided the ink with good film-forming ability and strong adhesion to fabrics. CNTs, dispersed in ethanol via sonication, were also introduced to enhance the mechanical toughness and wash stability of the conductive film. A short defoaming step ensured uniformity and smooth flow for subsequent coating.

The conductive ink was blade-coated onto a PET substrate and cured. Unlike conventional multi-step processes, our strategy integrated the conductive layer with the polyurethane matrix in a single thermal pressing step, without requiring additional adhesive or encapsulation layers. This method allowed high-quality transfer of the conductive patterns onto fabric surfaces, minimized leakage or migration of the LM, and significantly improved device stability and safety during wear.

Figure 2a–c showed the macro appearance and cross-sectional morphology of the conductive film on PET, revealing a uniform and flat surface with a clear layered structure (approximately 50 µm thick). As shown in Figure 2c, the conductive layer penetrates partially into the textile fibers, forming a mechanically interlocked structure that contributes to the stretchability and wash resistance of the device. Figure 2d presents the laser-patterned features with sharp and clean edges, demonstrating a minimum linewidth of 100 µm and high pattern fidelity.

Benefiting from the laser-assisted pretreatment, the proposed process enables stable and repeatable conductive patterning with

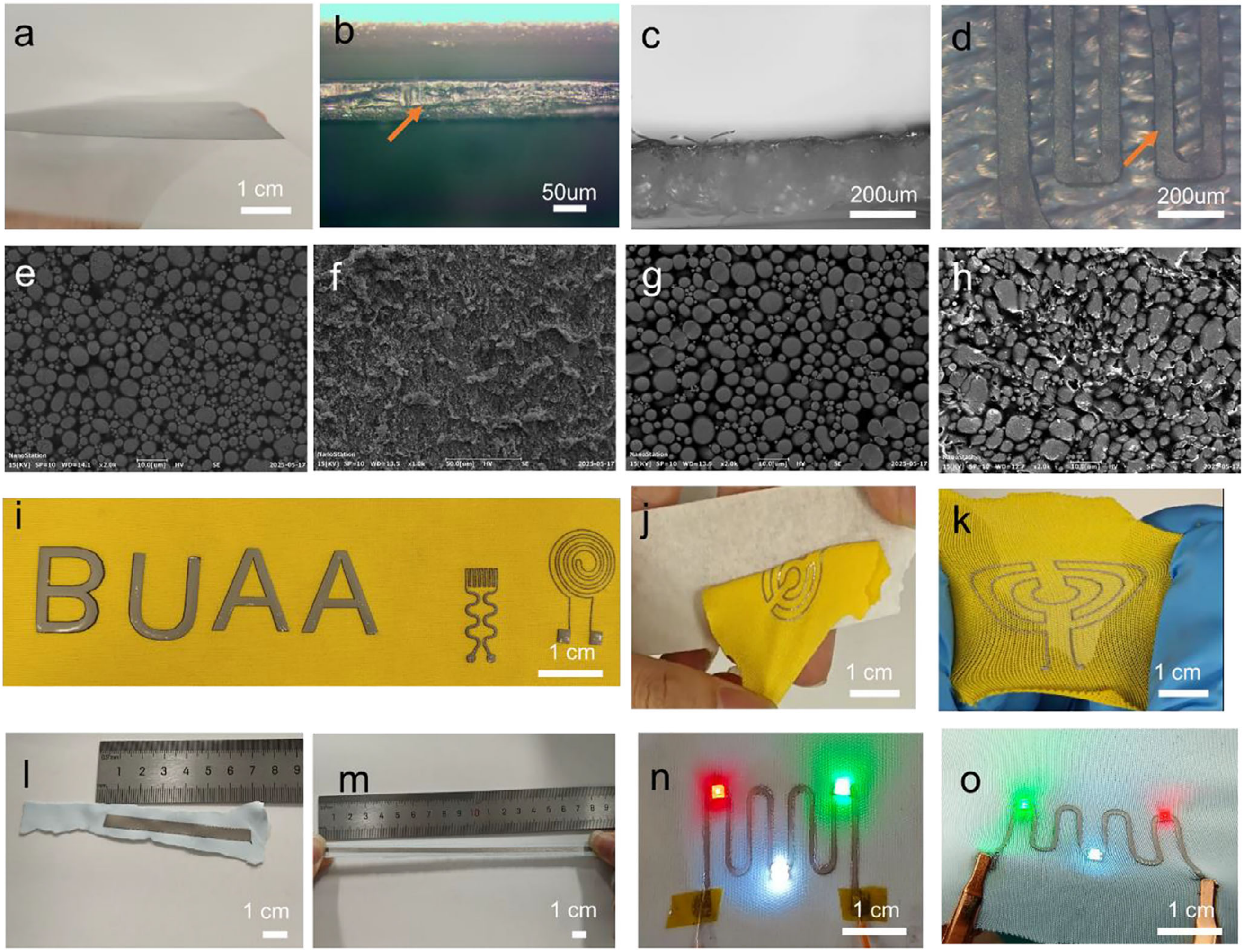

FIGURE 2 | Morphological and mechanical characteristics of patterned conductive textiles. (a) Optical image of the LM-based conductive film coated on PET, showing a uniform surface and high transparency. (b) Cross-sectional microscopic image of the conductive film with ~50 μm thickness and layered structure. (c) Cross-section after thermal transfer, indicating tight bonding and partial penetration into the textile. (d) Surface microscopic image of the transferred conductive pattern with clear edges and uniform geometry. (e) SEM image of the film before washing without CNT, showing intact morphology. (f) SEM image after washing without CNT, revealing delamination and surface damage. (g) SEM image before washing with CNT reinforcement. (h) SEM image after washing with CNT, showing improved surface stability and nanoparticle retention. (i) Optical demonstration of various customized patterns and logos enabled by laser cutting. (j) Tape-peeling test showing strong adhesion of the conductive film. (k) Tensile deformation test validating structural integrity under stretching. (l) Optical image of the fabric at its original length (before stretching). (m) Optical image of fabric stretched along the longer direction, withstanding up to ~130% strain. (n) LED circuit demonstration confirming continuous conductivity. (o) Lighting performance under mechanical stretching, validating electrical functionality under deformation.

a minimum achievable line width of approximately 100 μm. At this resolution, the patterned CNT/LM/TPU traces can be cleanly separated from the uncut regions and successfully transferred onto textile substrates without mechanical damage or electrical failure.

Although finer feature sizes are theoretically attainable by further narrowing the laser cutting width, practical limitations arise from laser-induced thermal effects and the compliant nature of textile-supported composite films. When the patterned lines become excessively narrow, separation from the surrounding regions during the transfer step becomes increasingly difficult, rendering the conductive traces susceptible to mechanical damage. Such limitations could potentially be alleviated through advanced cutting-pattern designs, such as widening the separation grooves to facilitate mechanical release; however, this aspect was not systematically investigated in the present work.

To evaluate the reinforcing effect of CNT, Figure 2e, f and Figure 2g, h compared the microstructure of conductive films with and without CNT before and after washing. While CNT addition did not significantly alter the size distribution of LM particles, it helped suppress structural delamination after washing, indicating improved interfacial stability. Figure 2i demonstrates the successful transfer of various complex patterns, including text, antenna designs, and electrode shapes, indicating the compatibility of this process with customized applications. Figure 2j, k demonstrates the robust adhesion and mechanical resilience of the fabric-based devices. Figure 2j shows that the conductive textile remains firmly attached to the substrate and cannot be peeled off even under tape tests, indicating strong interfacial adhesion. Figure 2k further reveals that, after being subjected to severe stretching and pulling, the textile can recover its original morphology without edge curling or permanent deformation, confirming its excellent structural integrity and conformability.

Figure 2l, m presents the photographic demonstration of the textile-based device before and after stretching, highlighting its good deformability and conformal behavior under tensile loading. The woven textile substrate permits strains of approximately 60% and 130% along its two principal directions, while the LM–polyurethane conductive film itself can sustain uniaxial strains exceeding 400%. These results indicate that the device can maintain reliable performance under typical wearable deformation scenarios and could adapt to even larger strains when integrated with more elastic fabrics. Figure 2n, o shows the textile device powering an LED under stretching, confirming its reliable conductivity and mechanical stability.

In summary, the patterned smart textile platform developed here offers excellent process controllability, design flexibility, and robust interfacial integration. This manufacturing approach provides a reliable and scalable foundation for subsequent multifunctional bioelectronic integration.

3.2 | Interfacial Compatibility and Chemical Composition Analysis

To further understand the composite mechanism and interfacial compatibility of the LM based conductive ink, FTIR was performed on different component systems, as shown in Figure 3a. Typical absorption peaks of TPU were observed in all samples, including the N—H/O—H stretching vibration near 3300 cm^{-1}, the C—H stretching vibration around 2900 cm^{-1}, and the C═O carbonyl stretching peak at approximately 1700 cm^{-1}. These results confirm that TPU serves as the main structural matrix and bonding phase in the system.

In the LM/TPU composite, although the LM itself does not contain infrared-active functional groups, the oxide layer Ga_2O_3 formed on its nanoparticle surface may interact with TPU through physical adsorption or mechanical interlocking, resulting in a relatively stable interface. This physical embedding and van der Waals adsorption mechanism helps the LM particles distribute uniformly within the polymer network, forming continuous and flexible conductive pathways.

With the introduction of carbon nanotubes CNT, the main FTIR spectra of the CNT/LM/TPU ternary composite (Figure 3a) do not show distinct new chemical bonds. However, the difference spectra (Figure 3b) reveal noticeable microstructural changes. In particular, there is a slight shift and enhancement in absorption intensity around 1700 cm^{-1} (C═O) and 1530 cm^{-1} (N—H bending), suggesting that the hydrogen bonding structures within the polyurethane chains may be locally reconfigured due to CNT addition. Additionally, enhanced absorption in the range of 1200–1000 cm^{-1}, associated with C—O—C stretching, further supports the strengthening of interfacial interactions. These changes can be attributed to possible hydrogen bonding and π–π stacking interactions between the residual carboxyl and hydroxyl groups on the CNT surface and the polar groups in TPU, such as N—H and C═O. The incorporation of these multiple interaction mechanisms not only improves the dispersion stability of the LM particles within the polymer matrix but also enhances the structural robustness of the device under conditions such as washing and mechanical stretching.

The CNT/LM/TPU composite undergoes partial softening and flows into the porous microstructure of the textile substrate. This process enables intimate contact between the conductive composite and individual textile fibers, forming a mechanically interlocked interface rather than a simple film–substrate boundary, resulting in a strong adhesion between the fabric and the conductive layer. To qualitatively evaluate the robustness of the interfacial adhesion, a manual tearing demonstration was performed. During this process, no interfacial delamination between the conductive layer and the textile substrate was observed. Instead, a fracture occurred with the conductive layer itself, while the bonding area remained firmly anchored to the textile fibers. A representative tearing and tensile fracture process is provided in Video S1, clearly showing cohesive failure of the conductive layer without observable interfacial separation. This observed failure mode qualitatively indicates that the interfacial adhesion is stronger than the cohesive strength of the conductive composite. Such mechanically interlocked adhesion is highly desirable for wearable electronic applications.

3.3 | Electrical, Mechanical, and Wash Stability Evaluation

To comprehensively evaluate the mechanical and electrical stability of the patterned conductive textile under realistic usage conditions, we conducted a series of performance tests, including assessments of static conductivity, washing durability, tensile behavior, and cyclic reliability. The results are summarized in Figure 3c–i.

The influence of LM content on electrical performance is shown in Figure 3c. As the LM volume fraction increases, the fabric's conductivity improves markedly, indicating that LM content is critical for establishing and maintaining conductive pathways. However, at excessively high LM concentrations, the polyurethane matrix fails to effectively encapsulate the LM, leading to leakage risks. Based on these findings, an optimal LM content of 15% was selected to balance conductivity and structural stability.

Washing durability is explored in Figure 3d, which tracks the resistance over repeated five washing cycles. In the absence of CNT, resistance increased sharply after the fourth cycle, and the sample eventually lost conductivity, likely due to mechanical damage and LM particle displacement caused by agitation. To further clarify this degradation behavior, optical microscopy images were captured after each washing cycle for both LM/TPU and CNT/LM/TPU samples in Figure S2. For the LM/TPU sample without CNT, fine stripe-like features appeared after the first washing cycle, indicating the onset of surface abrasion and LM redistribution. With continued washing, these features became

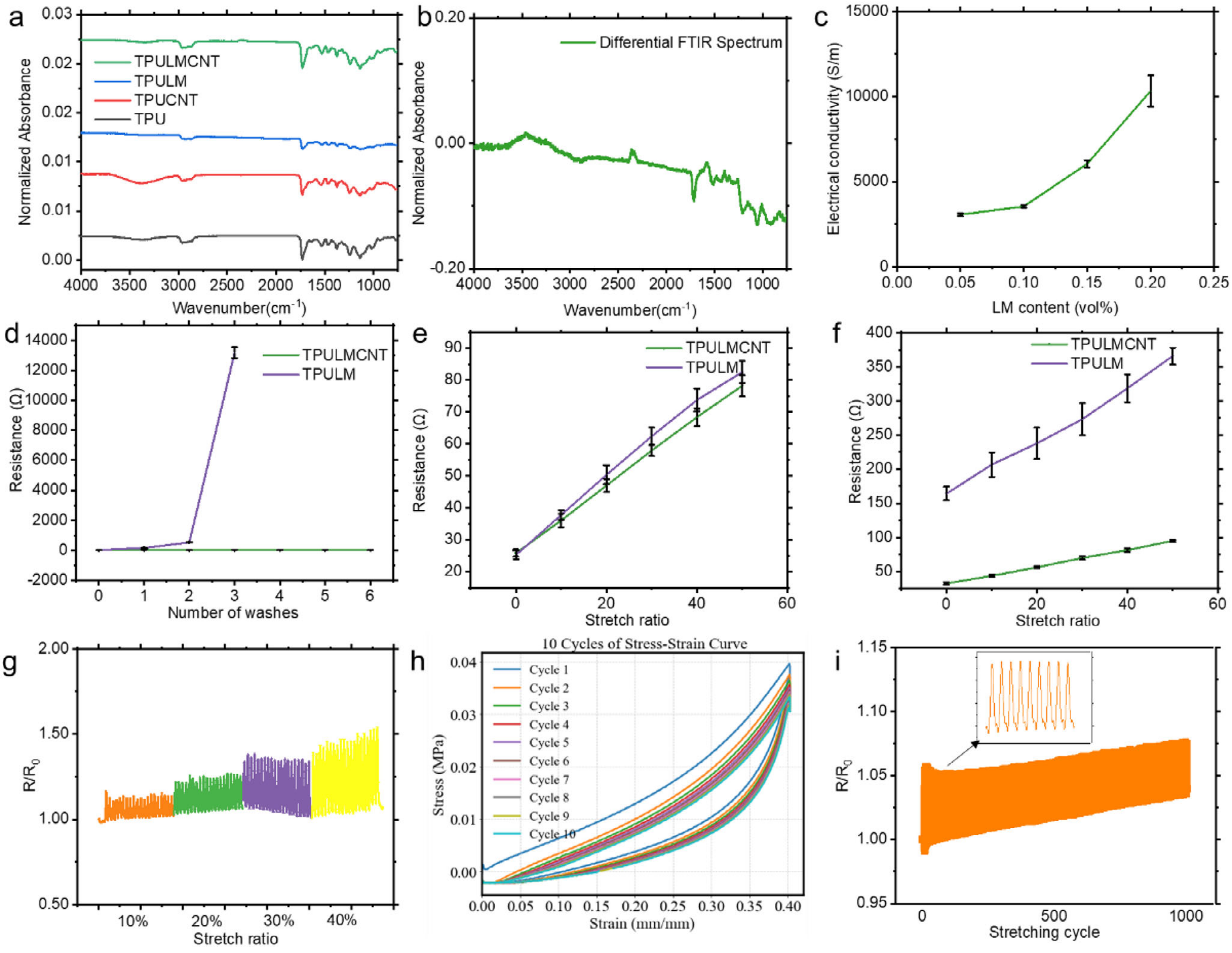

FIGURE 3 | Electrical and mechanical stability of the patterned LM-based conductive textile. (a) FTIR spectra of pristine TPU, LM/TPU, and CNT/LM/TPU. (b) Differential FTIR spectra highlighting spectral shifts. (c) Electrical conductivity of composites with different LM contents. (d) Resistance changes over multiple washing cycles for samples with and without CNT. (e) Resistance–strain curves (0–50% strain) before washing. (f) Resistance–strain behavior after one washing cycle. (g) Cyclic resistance response (R/R_0) of the conductive fabric under repeated stretching at different strain levels. The orange, green, purple, and yellow curves correspond to stretch ratios of 10%, 20%, 30%, and 40%, respectively. (h) Stress–strain curves over 10 tensile cycles up to 40% strain, demonstrating mechanical resilience. (i) Resistance retention over 300 cycles at 40% strain, confirming long-term electrical reliability.

more pronounced, reflecting progressive mechanical damage. Notably, visible microcracks emerged after the fourth cycle, marking a transition from surface abrasion to structural disruption of the conductive network. This morphological transition is in good agreement with the abrupt resistance increase observed in Figure 3d. After the fifth cycle, the cracks further deepened, leading to the complete loss of electrical continuity.

In contrast, the CNT-enhanced samples showed negligible resistance variation throughout the cycling tests, with no evidence of electrical failure. Consistently, no stripe or crack formation was observed in the CNT/LM/TPU samples even after five washing cycles, as shown in Figure S2, indicating effective suppression of abrasion and crack propagation induced by washing. These results suggest that CNTs serve as a reinforcing framework, enhancing LM particle anchoring and interfacial adhesion, thereby improving mechanical robustness during laundering. To further demonstrate the robustness and confinement of the conductive layer under wet and mechanical perturbations, representative tape-assisted peeling and water-washing processes are provided in Videos S2 and S3, respectively. In both cases, no liquid metal leakage, pattern delamination, or visible degradation was observed, supporting the stability of the encapsulation-free architecture during laundering.

Figure 3e compares the strain-dependent resistance behavior of both washed and unwashed samples. Within the 0–50% tensile range, both CNT and non-CNT groups showed comparable resistance increases, indicating that the addition of CNTs does not significantly alter the initial conductivity or strain sensitivity under mild deformation. Rather than affecting baseline performance, CNT primarily contributes under harsher conditions, such as post-wash or high-strain environments.

Post-washing tensile performance is highlighted in Figure 3f. The CNT-free sample displayed elevated baseline resistance and a rapid increase under strain, implying that washing had already disrupted the conductive network. In contrast, CNT-reinforced fabrics maintained low and stable resistance throughout stretching, closely resembling their pre-wash behavior. This confirms the protective role of CNT in maintaining structural and electrical integrity even after exposure to mechanical and fluid stress.

In addition to washing durability, the stability of the encapsulation-free architecture under wet and chemical environments relevant to wearable use was evaluated. To simulate perspiration in a controlled and quantitative manner, the samples were exposed to physiological saline for 24 h. Optical microscopy observations before and after saline exposure show that CNT/LM/TPU samples maintain intact and well-confined conductive patterns in Figure S3, whereas noticeable morphological degradation is observed in CNT-free samples.

These results indicate that the liquid metal is effectively confined within the CNT-reinforced polymer matrix and the porous textile structure, such that no additional encapsulation layer is required for stable operation under non-invasive wearable conditions on intact skin.

To assess long-term mechanical reliability, cyclic strain testing was conducted. Figure 3g presents the resistance response under repeated strain at four amplitudes: 0–10%, 0–20%, 0–30%, and 0–40%. At low to moderate strain levels (≤30%), the resistance cycles remain highly stable and repeatable, exhibiting negligible baseline variation and no electrical discontinuity, indicating that the conductive network can effectively withstand cyclic mechanical fatigue. When the strain amplitude is increased to 40%, a gradual upward shift in resistance is observed during cycling, which is attributed to progressive microstructural rearrangement of the conductive pathways under large deformation. Nevertheless, the resistance response maintains clear periodicity without abrupt signal failure, demonstrating preserved electrical functionality even near the upper strain limit. Further, Figure 3h shows the stress–strain profiles over ten stretch–release cycles. The curves largely overlap with minimal hysteresis, indicating excellent elastic recovery and structural resilience. Importantly, the introduction of the conductive coating does not compromise the intrinsic flexibility of the textile substrate.

Finally, Figure 3i presents the resistance evolution under repeated tensile cycling at a stretch ratio of 40%. Over extended cycling, a gradual upward shift in the resistance baseline is observed, accompanied by superimposed cyclic fluctuations. This behavior is attributed to progressive microstructural rearrangement of the conductive network under large, repeated deformation. Notably, even after 1000 stretch–release cycles, no abrupt resistance jumps, electrical discontinuity, or catastrophic failure are detected, indicating that the conductive composite maintains functional electrical integrity under prolonged mechanical fatigue.

3.4 | Validation of ECG Signal Acquisition Performance

Leveraging its high conductivity and skin conformity, the LM-based smart textile demonstrates strong potential for electrophysiological signal acquisition. In this work, we applied the textile electrode to ECG monitoring, evaluating its performance under both static and dynamic conditions, as illustrated in Figure 4.

Figure 4a shows the electrode design, featuring a circular sensing area connected to a strip-shaped conductive lead. This structure facilitates straightforward integration into garments for wearable applications. A representative electrode placement is depicted in Figure 4b, showing a bipolar electrode placement with textile electrodes positioned symmetrically over the upper left and right pectoral regions, simulating a simplified chest lead. Raw ECG data acquired during walking is shown in Figure 4c. The signal contains evident low-frequency drift and high-frequency noise, attributed primarily to motion artifacts. After applying bandpass filtering, the cleaned ECG waveform is presented in Figure 4d, with clearly identifiable R-wave cycles. The heart rate (HR) is measured at 98.5 bpm, and the RR interval standard deviation is 0.107 s, indicating good rhythm stability and signal quality. The extracted motion artifact component, isolated via low-pass filtering (<0.5 Hz), is provided in Figure 4e. The waveform displays smooth periodic undulations aligned with the user's walking rhythm, confirming its non-cardiac origin and successful removal through signal processing.

Frequency-domain analysis is summarized in Figure 4f, which compares the PSD of the raw signal, filtered ECG, and motion artifact. The unprocessed signal spans a wide frequency range dominated by low-frequency content. In contrast, the filtered ECG concentrates energy in the 1–20 Hz band, consistent with QRS complex frequencies, while the motion artifacts reside mainly below 1 Hz—validating the effectiveness of the filtering strategy. The corresponding time–frequency spectrogram of the raw ECG is shown in Figure 4g, where fluctuating low-frequency energy patterns further illustrate the presence of movement-induced artifacts.

To explore physiological responsiveness, two ECG segments collected under different activity states were analyzed. Post-exercise data (Figure 4h) shows an elevated heart rate of 144.5 bpm with a low RR interval standard deviation of 0.005 s, reflecting accelerated cardiac rhythm and reduced beat-to-beat variability. In contrast, the resting-state ECG (Figure 4i) exhibits a lower heart rate of 105.8 bpm and a higher RR interval standard deviation of 0.039 s, suggesting relatively greater rhythm variability at rest. These results demonstrate that the textile electrode can sensitively capture changes in heart rate and rhythm dynamics across activity states, while maintaining reliable signal acquisition during motion.

In practical wearable device applications, the humidity of the skin and sweat can significantly affect the contact interface between the electrodes and the skin, especially for dry textile electrodes. To evaluate the stability of the proposed unencapsulated liquid metal textile electrodes under different humidity conditions, a controlled sweating simulation experiment was conducted by introducing 1 milliliter of physiological saline on the electrodes and the contact fabric.

The electrochemical impedance measurement results before and after the salt water exposure are shown in Figure S4a. After adding the salt water, the impedance between the electrode and the skin significantly decreased, indicating that ion conduction

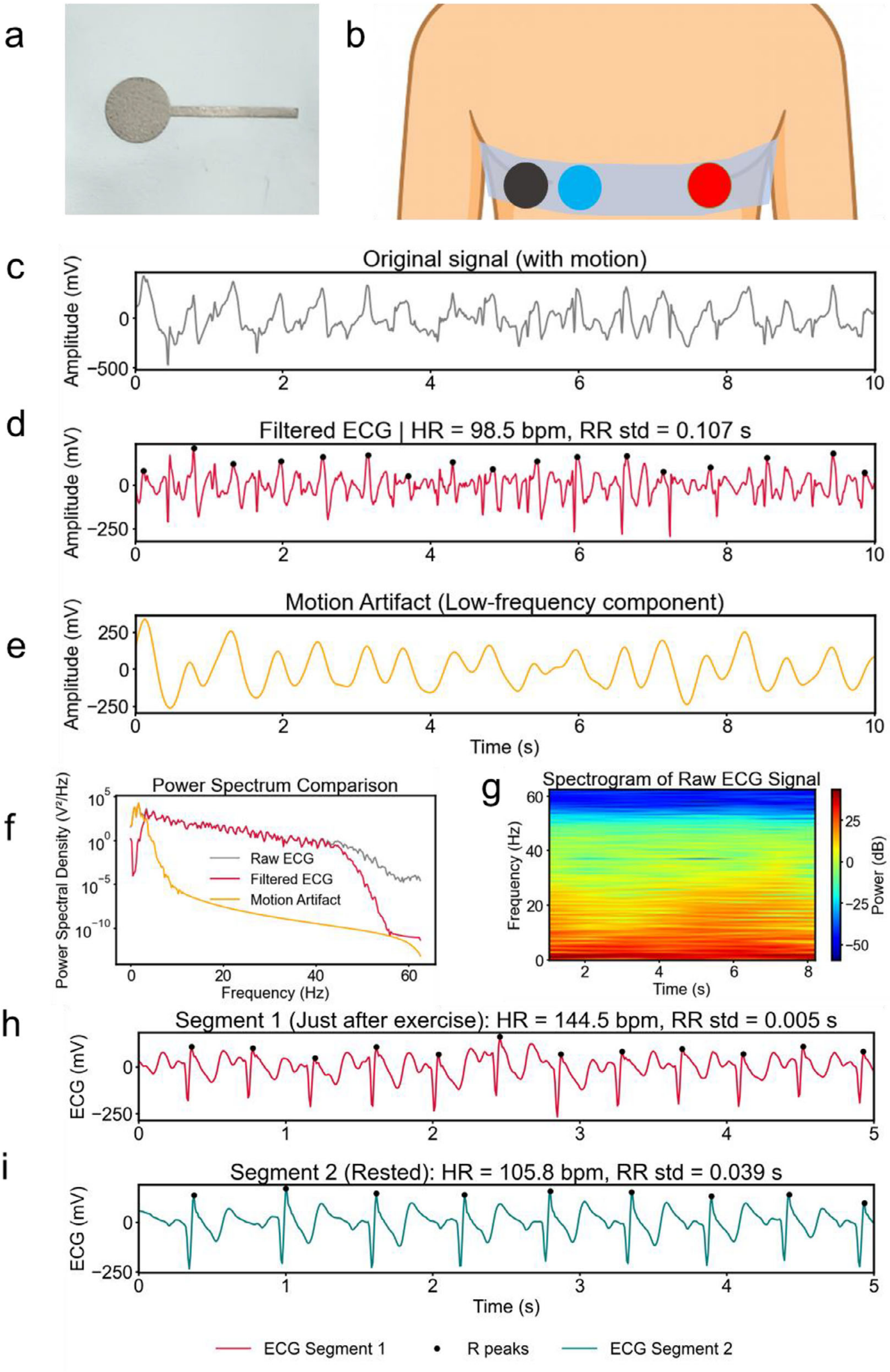

FIGURE 4 | Performance of the LM-based textile electrode in ECG monitoring. (a) Structure of the textile electrode featuring a circular sensing area and conductive lead. (b) Electrode placement on the chest is symmetrically positioned over the left and right chest regions to form a simplified bipolar lead. (c) Raw ECG signal acquired during walking. (d) Filtered ECG waveform showing clear R-wave cycles. (e) Extracted motion artifact component via low-pass filtering. (f) Power spectral density (PSD) comparison of raw ECG, filtered signal, and motion artifact. (g) Time–frequency spectrogram of the raw ECG signal. (h) ECG segment after exercise showing elevated HR (144.5 bpm) and low RR variability (0.005 s). (i) Resting-state ECG segment with reduced HR (105.8 bpm) and increased RR variability (0.039 s).

was enhanced and the contact resistance decreased under humid conditions.

However, although the impedance decreased, the electrocardiogram signals obtained under humid conditions did not show the corresponding improvement in signal quality. As shown in Figure S4b, although the characteristic electrocardiogram waveforms were still clearly distinguishable, the baseline fluctuations and noise increased compared to the dry conditions. This phenomenon indicates that for liquid metal-based electrodes, excessive moisture may introduce ionic polarization and lateral current diffusion at the electrode-skin interface, which may partially reduce the signal-to-noise ratio, although the impedance has decreased.

However, no signal interruption or severe waveform distortion was observed, and reliable electrocardiogram collection was maintained throughout the measurement process. These results indicate that the proposed textile electrodes can collect electrocardiogram data under different skin humidity conditions.

3.5 | Analysis of Heating Performance

To assess the feasibility of the LM-based textile device for thermal regulation and wearable warming applications, a serpentine-patterned heating element was fabricated, and its electrothermal behavior was systematically characterized through both experimental measurements and numerical simulations. The findings are summarized in Figure 5.

Figure 5a presents the measured temperature response curves under applied voltages ranging from 5 to 9 V. In all cases, the device exhibited a rapid temperature rise, stabilizing within approximately 30–40 s. The final steady-state temperature increased proportionally with voltage, reaching close to 49 °C at 9 V. These results demonstrate efficient Joule heating performance and controllable thermal output under low-voltage operation.

The corresponding simulation results are shown in Figure 5b, revealing temperature–time trends that align well with experimental data. The simulation model incorporates thermal conductivity of the LM circuit, heat capacity and diffusivity of the textile substrate, and convective heat loss to the surrounding air, thereby validating both the model's fidelity and the device design.

To further examine temperature uniformity, Figure 5c quantifies the spatial distribution of surface temperature under a 7 V condition after 30 s of heating. Temperature profiles along both the X and Y axes show a smooth, symmetric decay from the central region toward the edges. This pattern indicates effective in-plane heat spreading and thermal uniformity.

The evolution of heat distribution with increasing voltage is visualized in Figure 5d, e, which show simulated and experimental infrared thermal images, respectively, after 40 s of operation. In the simulation (Figure 5d), higher voltages resulted in elevated temperatures and larger effective heating areas along the serpentine circuit, with distinct color gradients indicating thermal accumulation along the conductive paths. The experimental images in Figure 5e reflect a similar progression: the heating traces were clearly visible, and the temperature increased steadily with voltage. The temperature at the fabric edges was slightly lower than predicted, attributed to factors such as textile porosity, air convection, or imperfect local contact. Despite these small differences, the overall experimental results agreed closely with simulation predictions, confirming the consistency and reliability of the heater's thermal performance.

In summary, the LM-based textile heater demonstrated rapid, stable, and spatially uniform Joule heating under low-voltage input. With a short warm-up time (<40 s), adjustable surface temperature (>45 °C), and high thermal uniformity, the device is well-suited for applications in smart garments, wearable therapeutic systems, and personal heating technologies.

To further evaluate the device performance under realistic conditions, we modeled the textile heater in direct contact with a human skin layer (thickness 3 mm, initial temperature 37 °C). Heat transfer at the interface was represented by an equivalent thin thermal resistance layer with a conductance of 300 $W{\cdot}m^{-2}{\cdot}K^{-1}$. As shown in Figure S5, the peak skin temperature beneath the heater increased by ~5.6–6.0 °C over 240 s. This indicates that the device can effectively transfer heat to the skin while maintaining physiologically safe temperature elevations. The inclusion of the skin layer in the simulation provides a more realistic assessment of on-body heating performance compared with idealized rigid or adiabatic substrates.

3.6 | Smart Glove Recognition System and Model Performance Analysis

To validate the practical applicability of the developed LM-based textile device in wearable human-machine interaction, we designed a smart glove system for gesture recognition, integrating flexible sensing, lightweight modeling, and embedded deployment. The system workflow and corresponding results are presented in Figure 6.

The structure of the smart glove platform is illustrated in Figure 6a, comprising four functional modules: signal acquisition, model training, embedded inference, and interactive control. Flexible strain sensors integrated into the glove detect resistance variations induced by finger movements, which are transmitted to a computer via a data acquisition board for feature extraction and model training. The trained model is then deployed onto a microcontroller unit (MCU), enabling real-time, low-power gesture recognition. While full interaction control was not implemented in this study, the system provides a modular and scalable architecture suitable for future application scenarios.

A schematic of the neural network used for classification is provided in Figure 6b. A lightweight multilayer perceptron (MLP) model was selected to strike a balance between accuracy and on-device efficiency. The model takes as input a 20-dimensional feature vector, consisting of mean, standard deviation, and the first eight FFT components from multiple signal channels. These features are processed by a three-layer fully connected network: the first layer contains 64 neurons with ReLU activation and batch normalization; the second layer contains 32 neurons; and

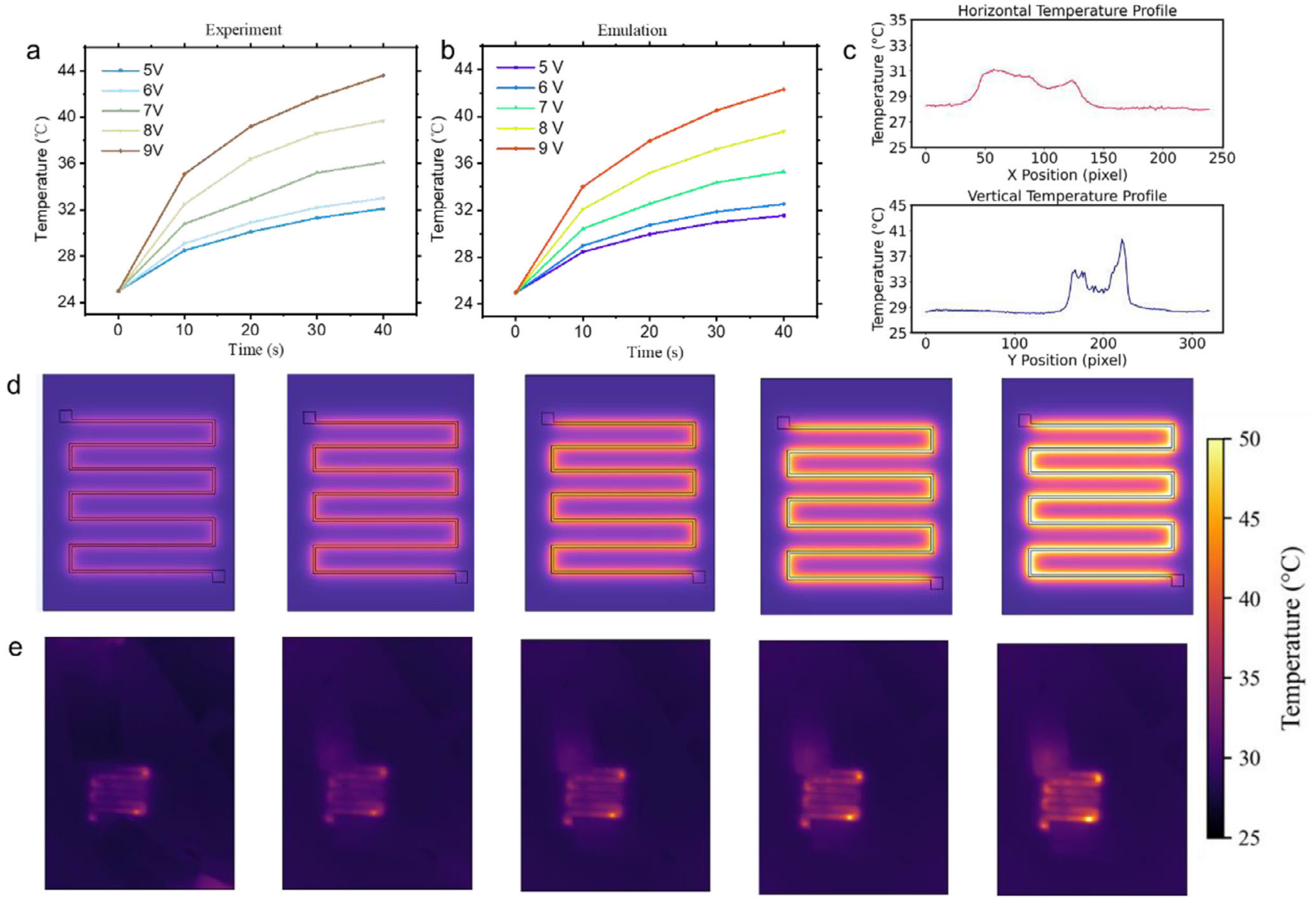

FIGURE 5 | Electrothermal performance of the LM-based textile heater. (a) Experimental temperature rise curves under applied voltages of 5–9 V. (b) Simulated temperature–time profiles under matching voltage conditions. (c) Quantitative temperature distribution along the X and Y directions after 30 s of heating at 7 V. (d) Simulated infrared thermal maps at different voltages after 40 s of operation. (e) Corresponding experimental thermal images under identical conditions, showing consistent temperature distribution and heating efficiency.

the final layer outputs probabilities over 10 gesture classes via Softmax. A dropout layer (rate = 0.3) is inserted between the first two layers to mitigate overfitting and improve generalization. This compact architecture supports fast training and efficient inference on resource-limited platforms.

Figure 6c displays images of the 10 static hand gestures used in the classification task, including both isolated and combined finger motions. Each gesture was recorded 120 times under standardized conditions, ensuring balanced class distribution and consistency across samples. For classification evaluation, the dataset was processed using a stratified five-fold cross-validation scheme. In each fold, approximately 80% of the samples from each gesture class were used for model training, while the remaining 20% were used for testing, ensuring balanced representation across all gesture categories. This process was repeated five times with different data partitions, and the final recognition accuracy was obtained by averaging the results across all folds.

To visualize the separability of gesture categories, Figure 6d presents a 2D projection of all samples using principal component analysis (PCA). Most gesture types form distinct clusters, particularly Classes 1, 2, 4, and 5. However, partial overlaps are observed among Classes 6, 7, and 9, suggesting that these classes may exhibit similar signal characteristics and require more expressive features or deeper temporal models to improve classification fidelity.

The training process is summarized in Figure 6e, where five-fold cross-validation results are shown. Both training and validation losses converge rapidly to below 0.1, while accuracy surpasses 95% within the first 10 epochs. The final training accuracy approaches 100%, and validation accuracy consistently remains above 97%, indicating excellent convergence and generalization performance.

Inter-feature relationships are examined in Figure 6f through a heatmap of pairwise correlation coefficients. The correlation between features varies considerably: R1_mean and R4_std are weakly correlated (−0.16), which can be advantageous for model generalization, whereas R3_mean and R5_mean exhibit high correlation (0.74), suggesting potential redundancy in feature representation. These insights may guide future feature selection or dimensionality reduction strategies.

Classification accuracy for each gesture is detailed in the confusion matrix shown in Figure 6g. Most classes are accurately predicted, with perfect classification observed in Classes 1, 2, and 4. Limited confusion exists between Classes 7 and 8, with a few

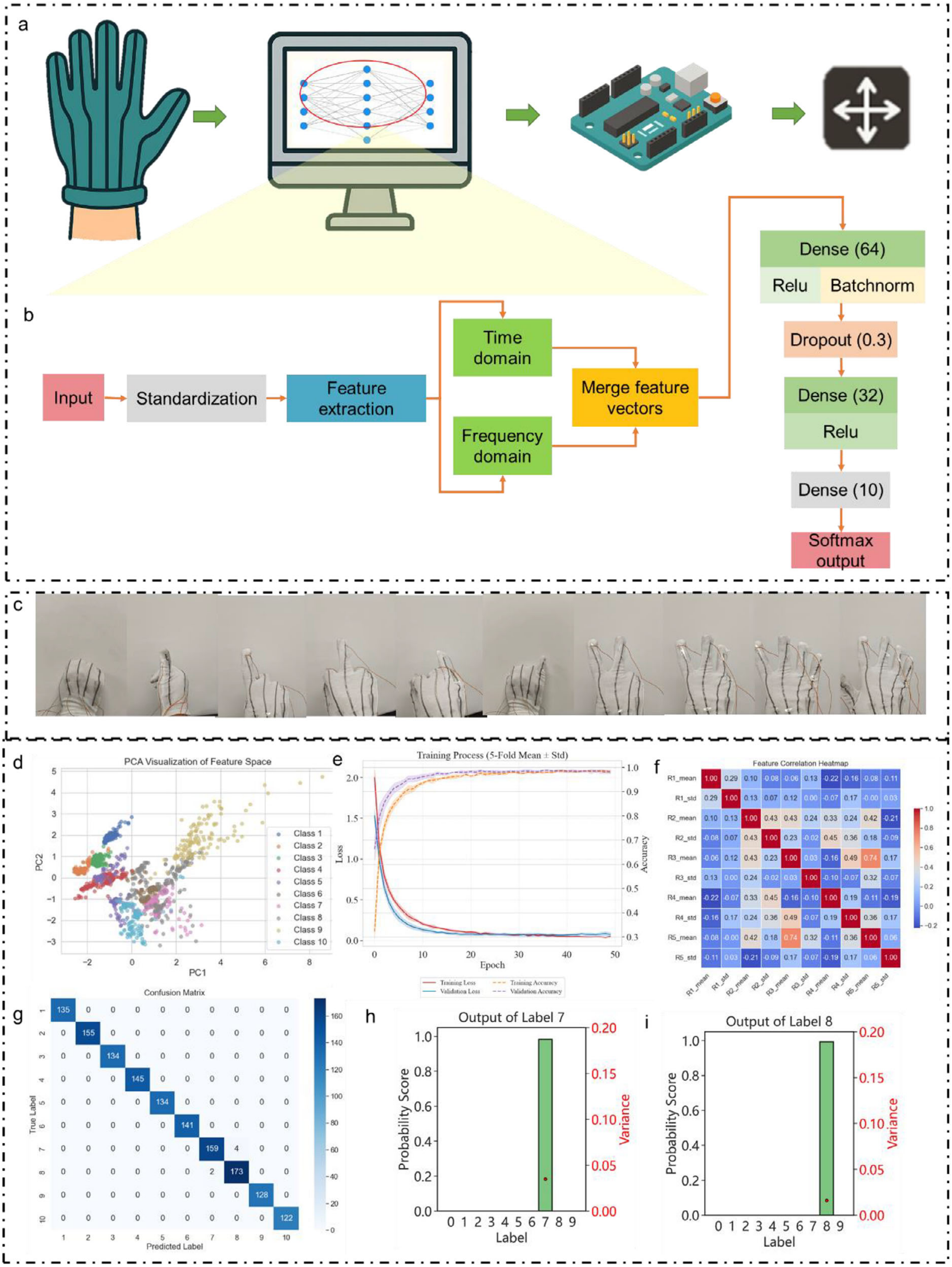

FIGURE 6 | System design and experimental validation of the smart glove for gesture recognition. (a) Architecture of the wearable gesture recognition system, including sensing, training, deployment, and interaction modules. (b) Structure of the lightweight MLP classification model based on time–frequency domain features. (c) Images of the 10 hand gestures used in the dataset. (d) PCA-based 2D distribution of gesture samples showing class separability. (e) Training and validation curves during five-fold cross-validation. (f) Feature correlation heatmap across different signal channels. (g) Confusion matrix of classification results with 10 gesture classes. (h) Predicted probability distribution for gestures 7 and 8. (i) Output variance indicating prediction uncertainty between similar gesture classes.

samples being misclassified between the two, likely due to similar motion profiles.

To further probe the model's behavior on ambiguous cases, Figure 6h, i analyze the predicted probabilities and output variance for Classes 7 and 8. While predicted probabilities remain high (close to 1.0), subtle increases in output variance reflect residual model uncertainty. These findings suggest potential for improvement through enhanced signal augmentation, incorporation of dynamic features, or use of temporal architectures to better capture transient gesture characteristics.

In summary, the smart glove system developed in this study combines flexible textile sensing and a compact neural network classifier to achieve accurate and responsive gesture recognition. This demonstrates the promising potential of textile electronics in wearable and intelligent interaction applications.

3.7 | Biocompatibility and Neural Electrical Stimulation Performance Evaluation

To assess the applicability of the LM textile electrodes in wearable medical scenarios, we conducted a comprehensive evaluation including biocompatibility assays, electrode–skin interface characterization, and simulation of stimulation performance, as summarized in Figure 7.

Figure 7a–c displays fluorescence images of NIH-3T3 fibroblasts stained with DAPI after incubation on different textile substrates. The LM/TPU sample (Figure 7a) and the CNT/LM/TPU composite (Figure 7b) both supported robust cell adhesion and proliferation, comparable to the control group without textile (Figure 7c). Across all groups, high cell density and uniform distribution were observed, with no visible signs of apoptosis or inhibitory aggregation.

Quantitative results are shown in Figure 7d, where the relative cell viability after 48 h of culture reached 99% for the LM/TPU group and 92% for CNT/LM/TPU, both comparable to the control (100%). These results confirm the low cytotoxicity of the textile electrodes and suggest their compatibility with skin-contacting and long-term wearable applications.

The physical appearance of the patterned textile electrode array is shown in Figure 7e. The array consists of 16 individually addressable rectangular electrodes (5 mm × 5 mm) fabricated through laser patterning followed by transfer printing onto a textile substrate.

Owing to its intrinsic flexibility and excellent skin conformability, the electrode array enables stable multi-channel electrical interfacing with the skin, providing a versatile platform for cutaneous electrical stimulation and bioelectrical signal acquisition.

In Figure 7f, we compare the impedance spectra of the textile electrode and a standard Ag/AgCl gel electrode across the frequency range of 1 Hz–10 kHz. While the textile electrode exhibits slightly higher impedance at low frequencies (<100 Hz) due to the absence of a liquid electrolyte, it performs comparably at higher frequencies. Its gel-free, reusable, and non-drying nature makes it particularly advantageous for long-term wearable stimulation and monitoring.

Figure 7g shows a representative potential waveform recorded from the skin surface during stimulation. The voltage signal exhibits a stable oscillatory pattern matching the input frequency, confirming that the textile electrode can effectively transmit electrical stimuli into subdermal tissue and generate a measurable surface potential field. These results collectively demonstrate the textile electrode's promising potential for neural modulation, rehabilitation, and electrophysiological feedback systems in wearable formats.

To clarify the electrode's working position, Figure 7h illustrates the multilayer structure of the skin and the electrode's contact on the epidermis. The stimulation signal is expected to propagate through the dermis, subcutaneous fat, and muscle layers to reach target nerves, where coupling efficiency and interface stability are critical to efficacy.

The spatial distribution of the electric field under 100 Hz, 5 V AC stimulation is shown in Figure 7i, simulated via COMSOL Multiphysics. The electric field is concentrated beneath and between electrodes along the skin surface, forming a symmetrical and continuous conduction pathway. The peak field strength reaches approximately 1.57×10^4 V/m, well within the safe and effective stimulation range for peripheral nerve activation.

Depth-dependent current density beneath the electrode center is plotted in Figure 7j, where current density increases steadily from ∼0.44 A/m^2 at the surface to ∼3.86 A/m^2 at 10 mm depth, with a secondary peak observed between 8–10 mm. This suggests efficient deep tissue penetration, highlighting the electrode's ability to activate deeper neural targets under low-voltage stimulation.

In contrast, Figure 7k shows the current density profile at the midpoint between electrodes ($z = 25.25$ mm). Here, current remains stable at ∼0.92 A/m^2 in the superficial 0–5 mm layer and gradually attenuates to ∼0.08 A/m^2 beyond that. A modest resurgence between 8–10 mm likely reflects lateral field effects or indirect conduction pathways, suggesting potential for shallow-to-intermediate depth modulation even in non-contact regions.

Although in vivo studies involving patient pain modulation or physiological response verification were not conducted in this work, and a functional interface for closed-loop stimulation-feedback remains to be developed, the present results demonstrate the strong potential of the proposed textile electrodes. The simulated electric field and current distributions confirm that effective stimulation can be achieved under low-voltage drive, with penetration sufficient to reach relevant neural structures. The inherent softness and conformability of the fabric platform provide a favorable basis for developing individualized, wearable electrostimulation systems.

4 | Conclusion

This study presents a high-stability fabric electronics platform based on LM, integrating stretchable conductivity, fast

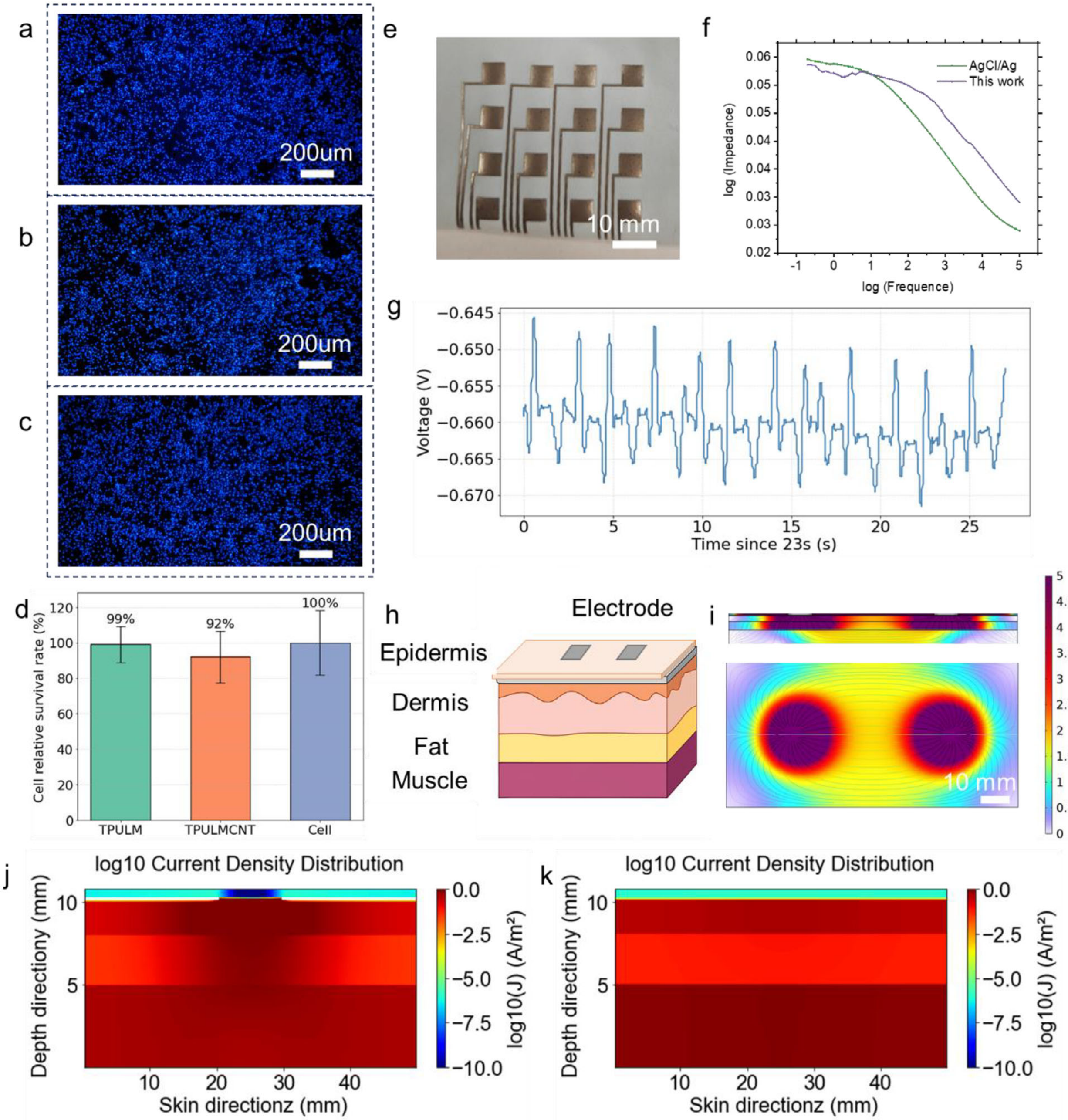

FIGURE 7 | Biocompatibility assessment and electrical stimulation performance analysis of LM fabric electrodes. (a–c) Fluorescence images of NIH-3T3 cells cultured on different textile samples. (d) Relative cell viability after 48-h incubation. (e) Photograph of the patterned textile electrode array. (f) Impedance spectra comparison between textile and Ag/AgCl electrodes. (g) Recorded surface potential during electrical stimulation. (h) Schematic of skin layers and electrode placement. (i) Simulated electric field distribution under AC stimulation. (j) Depth-wise current density beneath the electrode center. (k) Depth-wise current density between two electrodes.

thermal response, tactile sensing, and low-impedance stimulation. Optimized interfacial design ensures structural stability under repeated washing and deformation. Thermal experiments and simulations confirm rapid heating and uniform temperature distribution under low voltage, supporting wearable thermal regulation. A gesture recognition system combining embedded textile sensors and a lightweight neural network demonstrates high accuracy and robustness. Biocompatibility tests and interface modeling verify safe skin contact and effective electrical stimulation. Overall, this work provides a versatile and scalable approach for multifunctional wearable systems, with promising applications in digital health, rehabilitation, and human–machine interaction.

Acknowledgements

This research was funded by the National Natural Science Foundation of China (Grant Number. U23A20111 and 52474371), “111 Center”(Grant Number. B18002) and the Ningbo International Sci-tech Cooperation Projects (2024H009). The author gratefully acknowledges financial support from China Scholarship Council.

Conflicts of Interest

The authors declare no conflicts of interest.

References

1. J. Kim, R. Kumar, A. J. Bandodkar, and J. Wang, "Advanced Materials for Printed Wearable Electrochemical Devices: A Review," *Advanced Electronic Materials* 3 (2017): 1600260.

2. S. A. Han and M. Naqi, "All-Day Wearable Health Monitoring System," *EcoMat* 4 (2022): 12198.

3. S. Sreejith, L. M. I. Leo Joseph, S. Kollem, V. T. Vijumon, and J. Ajayan, "Biodegradable Sensors: A Comprehensive Review," *Measurement* 219 (2023): 113261.

4. D. He, D. Malu, and Y. Hu, "A Comprehensive Review of Indentation of Gels and Soft Biological Materials," *Applied Mechanics Reviews* 76 (2024): 050802.

5. P. Zhang, B. Zhu, P. Du, and J. Travas-Sejdic, "Electrochemical and Electrical Biosensors for Wearable and Implantable Electronics Based on Conducting Polymers and Carbon-Based Materials," *Chemical Reviews* 124 (2024): 722–767.

6. S. Shen, Q. Zhou, G. Chen, et al., "Advances in Wearable Respiration Sensors," *Materials Today* 72 (2024): 140–162.

7. R. Tamate, "Development of Functional Polymer Gel Electrolytes and Their Application in Next-Generation Lithium Secondary Batteries," *Polymer Journal* 57 (2024): 43–55.

8. X. Hong, W. Sun, S. Zhang, et al., "Washable and Multifunctional Electronic Textiles Via In Situ Lamination for Personal Health Care," *Advanced Fiber Materials* 6 (2024): 458–472.

9. H. C. Ates, P. Q. Nguyen, L. Gonzalez-Macia, et al., "End-to-End Design of Wearable Sensors," *Nature Reviews Materials* 7 (2022): 887–907.

10. M. B. Kulkarni, S. Rajagopal, B. Prieto-Simón, and B. W. Pogue, "Recent Advances in Smart Wearable Sensors for Continuous Human Health Monitoring," *Talanta* 272 (2024): 125817.

11. S. Yang and P. Sharma, "A Tutorial on the Stability and Bifurcation Analysis of the Electromechanical Behaviour of Soft Materials," *Applied Mechanics Reviews* 75 (2023): 044801.

12. X. Cheng, Z. Fan, S. Yao, et al., "Programming 3D Curved Mesosurfaces Using Microlattice Designs," *Science* 379 (2023): 1225–1232.

13. Z. Chen, W. Lin, C. Zhang, et al., "Multifunctional and Reconfigurable Electronic Fabrics Assisted by Artificial Intelligence for Human Augmentation," *Advanced Fiber Materials* 6 (2024): 229–242.

14. Y. Zhao, Y. Yuan, H. Zhang, et al., "A Fully Integrated Electronic Fabric-Enabled Multimodal Flexible Sensors for Real-Time Wireless Pressure-Humidity-Temperature Monitoring," *International Journal of Extreme Manufacturing* 6 (2024): 065502.

15. K. Chen, J. Xu, K. Yang, et al., "Highly Conductive and Elastic Electronic Silk Fabrics via 3D Textile Macro-design and Microscopic Plasma Activation for Personal Care and Information Interaction," *Advanced Fiber Materials* 7 (2025): 130–143.

16. Z. M. Abay, Y. Wei, Z. Tang, et al., "Versatile MXene/(GO-AgNWs) Electronic Textile Enabled by Mixed-Scale Assembly Strategy," *Nano Energy* 139 (2025): 110963.

17. F. Kang, Z. Wei, W. Tang, et al., "Multifunctional Electronic Fabrics Based on CNTs for Integrated Active Cooling and Pressure Sensing," *ACS Applied Nano Materials* 8 (2025): 14827–14840.

18. X. Yu, L. Chen, J. Zhang, et al., "Structural Design of Light-Emitting Fibers and Fabrics for Wearable and Smart Devices," *Science Bulletin* 69 (2024): 2439–2455.

19. W. Zhao, J. Natsuki, V. Dinh Trung, et al., "AgNPs/CNTs Modified Nonwoven Fabric for PET-Based Flexible Interdigitated Electrodes in Pressure Sensor Applications," *Chemical Engineering Journal* 499 (2024): 156252.

20. Z. G. Onses and N. B. Kiremitler, "Inkjet Printing of Aqueous Silver Inks on Water-Soluble Fabrics for Transient Electronics Applications," *ACS Applied Electronic Materials* 6 (2024): 5599–5607.

21. L. Zhu, X. Zhou, J. Zhang, et al., "Self-Adhesive Elastic Conductive Ink with High Permeability and Low Diffusivity for Direct Printing of Universal Textile Electronics," *ACS Nano* 18 (2024): 34750–34762.

22. J.-H. Ha, J. Ko, J. Ahn, et al., "Nanotransfer Printing of Functional Nanomaterials on Electrospun Fibers for Wearable Healthcare Applications," *Advanced Functional Materials* 34 (2024): 2401404.

23. B. Abdi, A. Tarhini, H. Baniasadi, and A. R. Tehrani-Bagha, "Developing Graphene-Based Conductive Textiles Using Different Coating Methods," *Advanced Materials Technologies* 9 (2024): 2301492.

24. H. Ghazal and L. Allam, "Conductive Polymer Coated Textile and Their Applications," *Journal of Textiles, Coloration and Polymer Science* 21 (2024): 313–331.

25. J. Zhao and Y. Peng, "Knot-Patterned Treble-Weaving Smart Electronic Textiles With Advanced Thermal and Moisture Regulation for Seamless Motion Monitoring," *Advanced Functional Materials* 0 (2025): 2501912.

26. C. Ye, L. Zhao, S. Yang, and X. Li, "Recent Research on Preparation and Application of Smart Joule Heating Fabrics," *Small* 20 (2024): 2309027.

27. W. Wu, X. Jin, A. Tiliman, et al., "A Flexible, Highly Sensitive, and Anti-Strain Interference Sensing Fabric Based on Conjugated Electrospinning Core–Shell Conductive Nanofiber Yarns for Ultra-Stable Pressure Sensing and Human–Machine Interaction," *Chemical Engineering Journal* 503 (2025): 158602.

28. S. Lee, D. H. Ho, J. Jekal, et al., "Fabric-Based Lamina Emergent MXene-Based Electrode for Electrophysiological Monitoring," *Nature Communications* 15 (2024): 5974.

29. W. Zhao, V. D. Trung, X. Hong, et al., "Textile-Based Interdigitated Electrode Piezoresistive Sensor: Materials, Fabrication and Applications - A Review," *Journal of Alloys and Compounds* 1014 (2025): 178764.

30. W. Zhao and L. Liu, "Thermomechanical Constitutive Models of Shape Memory Polymers and Their Composites," *Applied Mechanics Reviews* 75 (2022): 020802.

31. Z. Tang, W. Sun, C. Tao, et al., "Rapid Response, Superior Stable, and Durable Pressure Sensor With rGO/CNC Interdigital Electrode," *Nano Energy* 129 (2024): 110041.

32. W. Zhao, V. D. Trung, H. Li, et al., "Enhanced Functionalization of Nonwoven Fabric by Spray Coating AgNPs/CNTs Solution Prepared by a One-Step Method," *Chemical Engineering Journal* 494 (2024): 153101.

33. W. Zhao, V. D. Trung, J. Natsuki, J. Tan, W. Yang, and T. Natsuki, "Arterial Pulse Dynamics Monitoring via Ultrasensitive Sandwich Soft Electronics," *Advanced Fiber Materials* 7 (2025): 1615–1631.

34. W. Zhao, V. D. Trung, F. Li, et al., "Hierarchical Synergistic Engineering for Machine Learning-Assisted Gesture Recognition and Integrated Thermal Management," *Advanced Fiber Materials* 7 (2025): 1495–1513.

35. V. D. Trung, W. Zhao, J. Natsuki, J. Tan, W. Yang, and T. Natsuki, "Synergistic Interfacial Engineering for Ultrasensitive Bionic Tunable Strain Sensors With Robust Sensing Stability and Integrated Thermal Management," *Chemical Engineering Journal* 508 (2025): 161056.

36. Y. H. Hwang, H. Kim, and K. C. Choi, "Stretchable Fiber-Based Organic Light-Emitting Diodes Display Enabled by Robust, Conductive, and Deformable Via," *Advanced Science* 12 (2025): 14594.

37. S. Sohn, S. Kim, J. W. Shim, S. K. Jung, and S. Jung, "Printed Organic Light-Emitting Diodes on Fabric With Roll-to-Roll Sputtered ITO Anode and Poly(vinyl alcohol) Planarization Layer," *ACS Applied Materials & Interfaces* 13 (2021): 28521–28528.

38. S. Qiu, Y. Li, C. Dai, et al., "A Textile-Based Alignment-Free Electrophysiological Sensing Sleeve for Comprehensive Cardiovascular Monitoring," *Microsystems & Nanoengineering* 11 (2025): 228.

39. L. Tang, B. Lyu, D. Gao, Z. Jia, Y. Fu, and J. Ma, “A Janus Textile With Tunable Heating Modes toward Precise Personal Thermal Management in Cold Conditions,” *Small* 20 (2024): 2308194.

40. Y. Hou, Y. Yang, Z. Wang, et al., “Whole Fabric-Assisted Thermoelectric Devices for Wearable Electronics,” *Advanced Science* 9 (2022): 2103574.

41. Z. Liu, X. Hu, R. Bo, et al., “A Three-Dimensionally Architected Electronic Skin Mimicking Human Mechanosensation,” *Science* 384 (2024): 987–994.

42. Z. Zou, Y. Chen, S. Yuan, N. Luo, J. Li, and Y. He, “3D Printing of Liquid Metals: Recent Advancements and Challenges,” *Advanced Functional Materials* 33 (2023): 2213312.

43. J. Zhu, J. Li, Y. Tong, et al., “Recent Progress in Multifunctional, Reconfigurable, Integrated Liquid Metal-Based Stretchable Sensors and Standalone Systems,” *Progress in Materials Science* 142 (2024): 101228.

44. C. Cao, H. Su, L. Ai, et al., “Highly Stable Liquid Metal-Based Electronic Textiles by Adaptive Interfacial Interactions,” *Advanced Functional Materials* 34 (2024): 2409586.

45. L. Qiu, J. Li, Q. Yu, et al., “Liquid Metal Based Conductive Textile via Reactive Wetting for Stretchable Electromagnetic Shielding and Electro-Thermal Conversion Applications,” *Chemical Engineering Journal* 481 (2024): 148504.

46. H. Lin, H. Wang, Y. Yang, et al., “Smart Fabrics With Liquid Metal Reinforced PU/CNT/MXene Multilayer Structures for Constructing Multifunctional Sensors and Wearable Electronics,” *Journal of Materials Chemistry A* 12 (2024): 30872–30884.

47. Q. Zhuang, K. Yao, C. Zhang, et al., “Permeable, Three-Dimensional Integrated Electronic Skins With Stretchable Hybrid Liquid Metal Solders,” *Nature Electronics* 7 (2024): 598–609.

48. P. Bhuyan, M. Singh, Y. Wei, et al., “Thread-Analogous Elastic Fibers With Liquid Metal Core by Drawing at Room Temperature for Multifunctional Smart Textiles,” *Chemical Engineering Journal* 480 (2024): 147944.

49. J. He, Y. Xue, H. Liu, et al., “Humidity-Resistant, Conductive Fabric-Based Triboelectric Nanogenerator for Efficient Energy Harvesting and Human–Machine Interaction Sensing,” *ACS Applied Materials & Interfaces* 15 (2023): 43963–43975.

50. X. Wang, Q. Xu, J. Wang, P. Wang, and Y. Zhang, “Conductive Cotton Fabric Fabricated Using Stable Ag/MXene Colloidal Solution and PDMS for Heating and Electromagnetic Shielding,” *Materials Today Physics* 40 (2024): 101295.

51. H. Qiu, X. Qu, Y. Zhang, S. Chen, and Y. Shen, “Robust PANI@MXene/GQDs-Based Fiber Fabric Electrodes via Microfluidic Wet-Fusing Spinning Chemistry,” *Advanced Materials* 35 (2023): 2302326.

52. J. Tian, L. Mao, H. Cao, et al., “High-Performance Metallized Fabric-Based Flexible Conductive Patterns and Thermal Interface Materials,” *Chemical Engineering Journal* 523 (2025): 168980.

53. S. Ghosh, F. Meng, M. A. Shishir, M. Z. H. Ridoy, and J. Hu, “Development of Durable and Stretchable Hybrid Electronic Yarns for Temperature Measurement: Sensing and Mechanical Performance,” *Journal of Electronic Materials* 54 (2025): 9744–9770.

Supporting Information

Additional supporting information can be found online in the Supporting Information section.

Supporting File 1: smll72867-sup-0001-SuppMat.docx.

Supporting File 2: smll72867-sup-0002-VideoS1.mp4.

Supporting File 3: smll72867-sup-0003-VideoS2.mp4.

Supporting File 4: smll72867-sup-0004-VideoS3.mp4.